RESEARCH ARTICLE

DOI:10.61558/2993-074X.3474 **Article ID:** 1006-3471(2024)00-0000-00

Http://electrochem.xmu.edu.cn

Electrochemical-Method-Induced Strong Metal-Support Interaction in Pt-CNT@SnO_2 for CO-Tolerant Hydrogen Oxidation Reaction

Shen-Zhou Li [a,+], Zi-Jie Lin [a,+], Qi-An Chen [a,+], Zhao Cai [b] and Qing Li [a,*]

[+] Equal contributions

a State Key Laboratory of Materials Processing and Die & Mould Technology, School of Materials Science and Engineering, Huazhong University of Science and Technology, 1037 Luoyu Road, Wuhan, 430074, Hubei, China. E-mail: qing_li@hust.edu.cn

b Faculty of Materials Science and Chemistry, China University of Geosciences (Wuhan), Wuhan 430074, China

Supporting information for this article is given via a link at the end of the document.

Keywords: Strong metal-support interaction • Pt • supported metal catalyst • hydrogen oxidation reaction • CO tolerance

Abstract: Inducing the classic strong metal-support interaction (SMSI) is an effective approach to enhance the performance of supported metal catalysts by encapsulating the metal nanoparticles (NPs) with supports. Conventional thermal reduction method for inducing SMSI processes is often accompanied by undesirable structural evolution of metal NPs. In this study, a mild electrochemical method has been developed as a new approach to induce SMSI, using the cable structured core@shell CNT@SnO_2 loaded Pt NPs as a proof of concept. The induced SnO_x encapsulation layer on the surface of Pt NPs can protect Pt NPs from the poisoned of CO impurity in hydrogen oxidation reaction (HOR), and the HOR current density could still maintain 85% for 2000 s with 10000 ppm CO in H_2, while the commercial Pt/C is completely inactivated. In addition, the electrons transfer from SnO_x to Pt NPs improved the HOR activity of the E-Pt-CNT@SnO_2, and the excellent exchange current density is 1.55 $A \cdot mg_{Pt}^{-1}$. In situ Raman spectra and theoretical calculations show that the key to the electrochemical-method-induced SMSI is the formation of defects and the migration of SnO_x caused by the electrochemical redox operation and the weakening the Sn-O bond strength by Pt NPs.

Introduction

The classical strong metal-support interaction (SMSI), which has been extensively studied in supported metal catalysts, refers to the encapsulation effect of the support material on metal particles under specific conditions.[1-4] In 1978, Tauster et al. discovered that the adsorption behavior of CO on the TiO_2 supported Pt nanoparticles (NPs) catalyst was significantly changed after annealing in H_2, and named this phenomenon as the “strong metal-support interaction”.[5] In recent years, with the advancement of characterization techniques, it has been gradually recognized that these changes in catalytical properties should be attributed to the evolution of catalyst structure.[6, 7] During the reductive thermal treatment conditions, the support materials would migrate and form a thin amorphous encapsulation layer on metal NPs. This encapsulation structure modifies the catalytic site of the metal NPs, and could imparts unique catalytic properties of the catalysts, especially in the adsorption of reactants and reaction intermediates, which on account of the electronic effect of synergistic effect. [8-13]

The most commonly used method to induce SMSI is thermal reduction. However, the harsh conditions of thermal reduction method (usually above 773 K) usually induce additional structural evolution of the supported catalysts, such as metal NPs growth/ripening and alloying with the elements of supports.[14-16] Some efforts have been devoted to induce SMSI under mild conditions. Inducing SMSI typically requires two processes: creating defects of supports and facilitating atomic migration.[17, 18] Dai et al. utilized ultraviolet (UV) radiation to stimulate the photocarrier in TiO_2 and lead to the formation of Ti^{3+} species and oxygen vacancies, thereby achieving encapsulation of Pt NPs.[19] Moreover, high-speed particle collisions and shock waves during ultrasound treatment could cause surface damage and oxygen vacancies in TiO_2, also resulting in SMSI.[20] Electrochemical method is also an gentle and controllable way to induce SMSI . Strasser et al. proposed the electrochemical-method-induced SMSI in Pt-$RuTiO_x$ system and the encapsulation of Pt by oxides was demonstrated.[21] The encapsulation structure suppressed the catalytic activity towards oxygen reduction reaction (ORR) as it impeded the O_2 transport to the Pt surface.[22-25] Although the electrochemical-method-induced SMSI exhibits unique electrochemical behavior, the mechanism still needs further in-depth exploration. Additionally, since the thin encapsulation layer on the metal NPs does not have a blocking effect on small molecules such as H_2, the SMSI-derived catalysts hold promise for hydrogen electrocatalysis, which has not been studied yet.

Herein, we demonstrate an electrochemical method to induce the SMSI on core@shell structured CNT@SnO_2 supported Pt NPs (Pt-CNT@SnO_2) and the encapsulated Pt NPs (E-Pt-

CNT@SnO_2) exhibits excellent hydrogen oxidation reaction (HOR) activity and CO-tolerance. After a certain CV scanning treatment (0.05-1.2 V vs. RHE, 200 cycles), amorphous SnO_x encapsulation was observed on the surface of Pt NPs while the adsorption of CO on Pt surface was reduced, which proved the occurrence of SMSI. The obtained E-Pt-CNT@SnO_2 catalyst exhibits an excellent exchange current density of 1.55 A·mg_{Pt}^{-1} for HOR, higher than that of the commercial Pt/C (1.24 A·mg_{Pt}^{-1}) and Pt-CNT@SnO_2 (1.22 A·mg_{Pt}^{-1}). Impressively, the elective permeability (penetrating H_2 but blocking CO and O_2) of SnO_x encapsulation layer make E-Pt-CNT@SnO_2 has great CO tolerance and can still maintain an 85% of current density in the presence of 10000 ppm CO after 2000 s. Theoretical calculations and in-situ Raman spectra results reveal that the supported Pt NPs could extract electrons from SnO_2 supports and reduce the bond order of Sn-O bonds, thereby weakening the Sn-O bond strength and promoting the migration of SnO_x to form encapsulation.

Experimental Section

Preparation of catalysts

Synthesis of CNT@SnO_2: 10 mg CNTs were dissolved in 40 mL hydrochloric acid with pH = 1 under ultrasonic dispersion for half an hour. Then 1 g of anhydrous $SnCl_2$ was added and sealed with polyethylene film. The reaction was performed at 60 °C for 3h, and then centrifuged with deionized water and ethanol. The CNT@SnO_2 was obtained after freeze-drying.

Synthesis of E-Pt-CNT@SnO_2: 16 mg as-prepared CNT@SnO_2-T was dispersed in a mixture of ethylene glycol and water, and 1 mL of 10 mg·mL^{-1} chloroplatinic acid solution was added to the mixture. Finally, the ratio of ethylene glycol to water was controlled to 3:1. The mixture was stirred and reflow at 130 °C for 1 h. The final catalyst Pt-CNT@SnO_2 was obtained by centrifugation and freeze drying and the loading of Pt is 9.78 wt.%. Then the catalyst was loaded on carbon glass electrode followed by cycling the potential between 0.05 and 1.05 V_{RHE} at a scan rate of 200 mV·s^{-1} in N_2-saturated 0.1 M $HClO_4$ to finally obtain E-Pt-CNT@SnO_2.

Electrochemical Measurements

Electrochemical measurements were performed with 3-electrode system on CHI760e electrochemical workstation (Shanghai Chenhua Instrument Corporation, China). Glassy carbon rotating disk electrode was used as a working electrode (5 mm in diameter), Ag/AgCl (saturated KCl) as a reference electrode and graphite rod as a counter electrode. All potentials were experimentally converted to values with reference to a reversible hydrogen electrode (vs. RHE).

Pt-C, Pt-CNT@SnO_2 were dispersed in a mixture containing water, isopropanol and Nafion (5%) (v/v/v = 1:1:0.1) to form a 1 mg·mL^{-1} ink. Ink was cast on the glassy carbon and dried under ambient condition. The final loading of the Pt was kept at about 10 μg_{Pt}·cm^{-2} (determined by ICP-MS).

The CV measurements were performed in N_2-saturated 0.1 M $HClO_4$ solutions at a scan rate of 50 mV·s^{-1}. The HOR polarization curves were measured in H_2-saturated 0.1 M $HClO_4$ using a rotating disk electrode (RDE) at a rotation rate of 400 - 2500 rpm and a sweep rate of 1 mV·s^{-1}.

For CO stripping measurements, pure CO gas at an ambient pressure was bubbled into 0.1 M $HClO_4$ for 30 min while holding the potential at 0.1 V_{RHE}. After the electrolyte was purged with Ar gas for 30 min to completely remove residual CO molecules in the electrolyte, CO-stripping curves were obtained in Ar-saturated electrolyte with a scan rate of 20 mV·s^{-1} at room temperature and in the potential range of 0.05 - 1.2 V_{RHE}. The electrochemical surface areas (ECSA) was calculated by integrating the currents in the underpotential deposition region of hydrogen and CO oxidation peak region, assuming a monolayer H_2 charge of 210 μC·cm^{-2} and a monolayer CO charge of 420 μC·cm^{-2}.

Kinetic current density (j_k) could be deduced from the Koutecky-Levich equation:

$$\frac{1}{j}=\frac{1}{j_k}+\frac{1}{j_d}=\frac{1}{j_k}+\frac{1}{Bc_0\omega^{1/2}} \quad (1)$$

where j, B, c_0, and ω are the measured current density, the Levich constant, the solubility of H_2 (7.33×10^{-4} mol·L^{-1}), and the speed of the rotating, respectively. Exchange current density (j_0) could be extracted from the Butler-Volmer equation:

$$j_k = j_0\left[e^{\frac{\alpha F}{RT}\eta} - e^{\frac{-(1-\alpha)F}{RT}\eta}\right] \quad (2)$$

j_0 could be also obtained from the approximate Butler-Volmer equation:

$$j = j_0\frac{\eta F}{RT} \quad (3)$$

where α, η, R, T and F represent the transfer coefficient, the overpotential, the universal gas constant (8.314 J·mol^{-1}·K^{-1}), the temperature in Kelvin (298 K) and the Faraday constant, respectively

Physicochemical Characterizations

TEM images were taken from a FEI Tecani G2 20 with an operation voltage of 200 kV. HRTEM images were taken from a FEI Tecani G2 F30 with an operation voltage of 300 kV. The HAADF-STEM characterization was conducted on a JEOL JEMARM200F STEM/TEM with a guaranteed resolution of 0.08 nm. XRD were collected from Rigaku MiniFlex 600 diffractometer with a Cu radiation source (λ = 0.15406 nm). XPS spectra were collected from AXIS-ULTRA DLD-600W. ICP-MS result was carried out from ELAN DRC-e. EPR spectra were acquired on a Bruker EMXplus spectrometer. In situ Raman measurements were performed on Renishaw invia with 532 nm excitation wavelength and a 50× microscope objective. Raman frequency was calibrated by a Si wafer during each experiment. In situ electrochemical Raman experiments were employed in a Raman cell (Gaoss Union) and potentiostat (CHI 760e) was used to control the potential.

First Principles Calculations

All the first principles calculations are performed with density-functional theory (DFT) implemented in Vienna *ab initio*

simulation package (VASP)[26] using the projector augmented-wave method[27]. The valence electron wave functions are expanded on the plane-wave basis sets with a kinetic energy cutoff of 400 eV. The electronic exchange-correlation functional is in the Perdew-Burke-Ernzerhof (PBE) form[28] with generalized gradient approximations. Based on the convergence test, the K-points sampling in first Brillouin zone employ Monkhorst-Pack scheme[29] with a 1×1×1 mesh. The SnO_2 slab model was constructed based on the SnO_2(101) surface model in a 4×2 in-plane supercell. The adjacent slabs were separated by a 15 Å vacuum in the normal direction. The COHP analysis was performed by using the LOBSTER software.[30]

Results and Discussion

Structural analysis

The schematic illustration of catalyst preparation process is shown in **Figure 1**a. The SnO_2 coated CNTs were prepared by a precipitation method that the Sn^{2+} precursor nucleated and oxidized into SnO_2 at the carbonyl group of CNTs. The obtained CNT@SnO_2 presents a cable structure, and the CNT is effectively sealed by an external SnO_2 layer (Figure 1b and Supporting Information Figure S1). Then, Pt NPs were supported on the CNT@SnO_2 by a glycol reduction method and named as Pt-CNT@SnO_2. The average size of Pt NPs in Figure 1c and Supporting Information Figure S2 is 3.18 ± 0.62 nm. Finally, CV scanning on the Pt-CNT@SnO_2 with the potential range of 0.05-1.2 V vs. RHE was executed to induce the SMSI, and the final catalyst was obtained after 200 cycles (denoted as E-Pt-CNT@SnO_2). As shown in Figure 1d and Supporting Information Figure S3, the overall structure and the average particle size of Pt NPs of E-Pt-CNT@SnO_2 have no obvious change after the electrochemical treatment. In addition, X-ray diffraction (XRD) patterns of the catalysts are shown in Figure 1e and the peaks located at 26.6°, 33.9°, and 51.8° corresponds to the rutile SnO_2 (space group P42/*mnm*, JCPDS PDF 41-1445), while the peaks located at 39.8°, and 46.2° corresponds to the fcc Pt(space group Fm-3m, JCPDS PDF 04-0802). The particles size can be calculated by Scherrer formula and the grain sizes of SnO_2 and Pt are ~4.2 nm and ~3.6 nm,[31] respectively, which is consistent with the result of TEM.

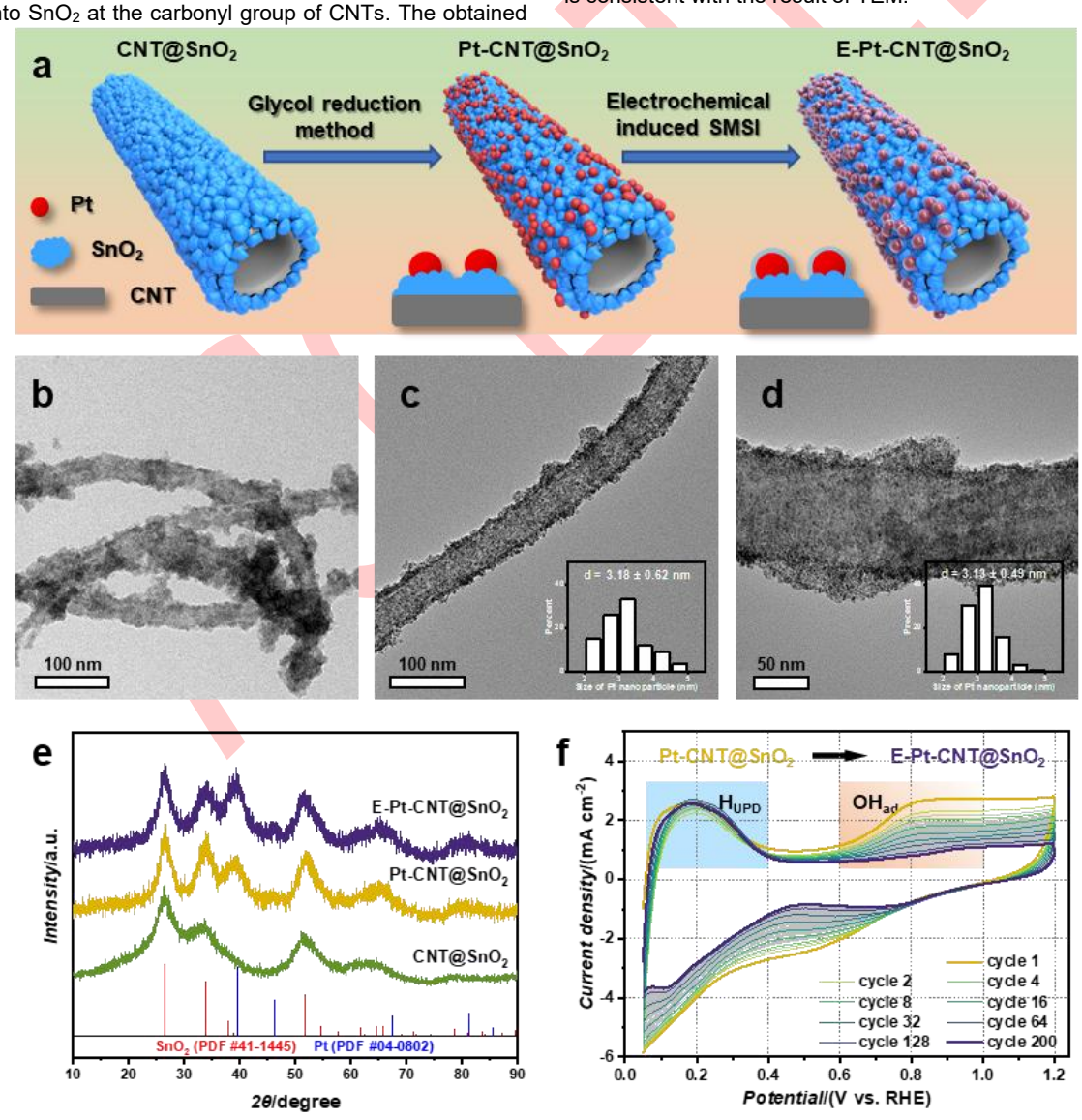

Figure 1. (a) Schematic illustration of the synthetic route to E-Pt-CNT@SnO_2. HRTEM image of the(b) CNT@SnO_2, (c) Pt-CNT@SnO_2, and (d) E-Pt-CNT@SnO_2. Inset: statistical distribution of Pt particle size. (e) XRD patterns of the CNT@SnO_2, Pt-CNT@SnO_2, and E-Pt-CNT@SnO_2. (f) CV curves of the process of the electrochemical-induced SMSI.

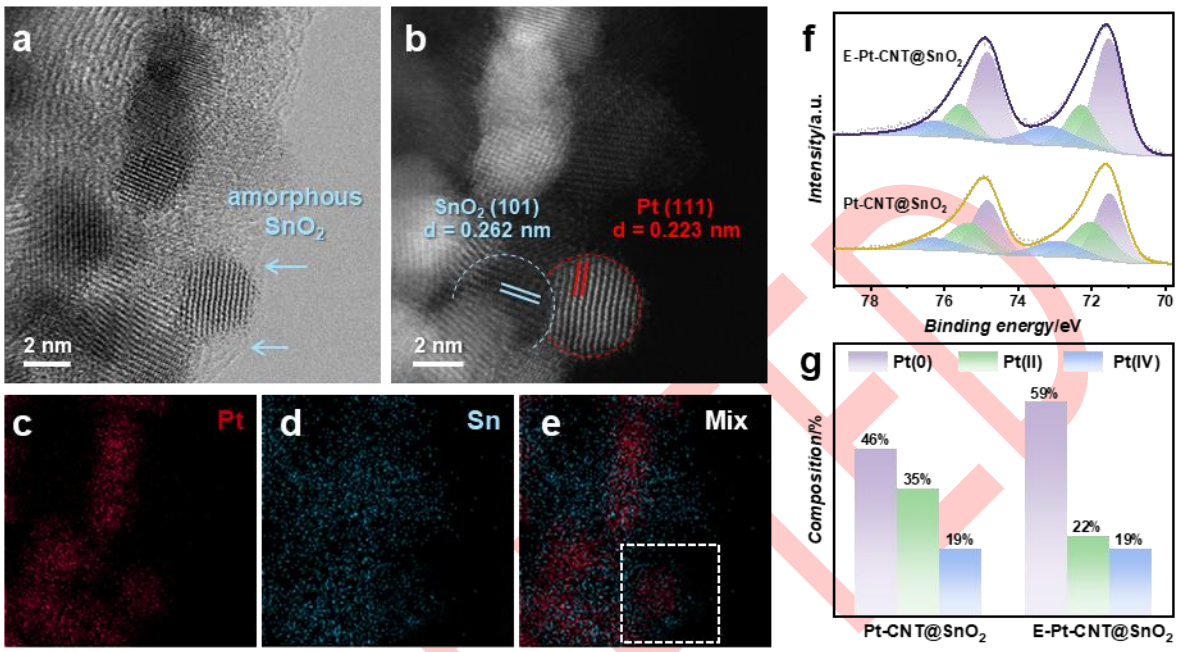

Figure 2. (a) HAADF-STEM images of E-Pt-CNT@SnO_2 for (a) bright field and (b) dark field. EDS-elemental mappings of (c) Pt, (d) Sn and (e) mix sample. (f) High-resolution Pt 4f XPS spectra of E-Pt-CNT@SnO_2 and Pt-CNT@SnO_2. (g) The composition of the Pt(0), Pt(II), and Pt(IV).

The curves of CV scanning for Pt-CNT@SnO_2 is shown in Figure 1f, and it should be noted that the electrochemical behavior of the catalyst changes significantly as the electrochemical cycling proceeds. The region of underpotential deposition of hydrogen (H_{UPD}) has a little change, but the region of OH adsorption (OH_{ad}) is significantly reduced. At the beginning of CV scanning proceeds, an obvious shrinking of the OH_{ad} region could be observed in each cycle, and then the shrinking rate gradually slowed down. After 128 cycles, the CV curve tended to be stable, indicating the stabilization of the structure and the preparation of E-Pt- CNT@SnO_2. This unusual electrochemical behavior could be attributed to encapsulation of Pt NPs by the amorphous SnO_x layers during electrochemical cycling, that is, the electrochemical-induced SMSI. It has been studied that the thin oxide encapsulation layer acts as shielding layer to hinders the oxygen intermediates to adsorption on the Pt surface,[32] but this thin oxide encapsulation layer doesn't interfere with the transfer of H_2 or protons.

High-angle annular dark-field scanning transmission electron microscopy (HAADF-STEM) is employed to characterize the nanostructures of E-Pt-CNT@SnO_2. As shown in **Figure 2**a-b, the Pt NPs of E-Pt-CNT@SnO_2 are in contact with the crystalline SnO_2 on the support, while some amorphous material exists around the Pt NPs. The spacings of lattice fringes are 0.262 nm and 0.223 nm, corresponding to (101) facets of SnO_2 and (111) facets of Pt, respectively, indicating that CNT@SnO_2 supports does not exert significant stress on Pt. In the energy dispersive spectroscopy (EDS) elemental mapping (Figure 2c-e), a faint signal of Sn around the Pt NPs proves that the amorphous material is SnO_x. Meanwhile, X-ray photoelectron spectroscopy (XPS) analysis indicates that there is no shift in the Pt 4f peak position of E-Pt-CNT@SnO_2 and Pt-CNT@SnO_2 (Figure 2f and Supporting Information Figure S4). However, the composition of Pt(0) increases from 46% to 59% after encapsulation in Figure 2g. This can be attributed to the fact that the encapsulation of Pt NPs increases the contact area between Pt and SnO_x, which enhances the electronic metal-support interaction (EMSI). Consequently, more electrons are transferred from SnO_x to Pt NPs, leading to a reduction in the oxidation state of Pt.

Electrochemical process analysis

To further explore the electrochemical properties of E-Pt-CNT@SnO_2, a series of electrochemical tests were conducted. Initially, CO-stripping tests were performed and CO could be utilized as a molecule probe to examine the surface state of Pt. The CO-stripping result for commercial Pt/C is illustrated in **Figure 3**a. During the first cycle (solid line) of the scanning process, there is no significant H_{UPD} region observed and a

sharp CO oxidation peak appeared around 0.76 V due to the surface of Pt being occupied by CO molecules. As CO is oxidized to CO_2, the surface of Pt is re-exposed, resulting in the appearance of normal signals of H_{UPD} and OH_{ad} region during the second cycle (dashed line) of scanning. The E-Pt-CNT@SnO_2 exhibits a distinctive result for CO-stripping tests (Figure 3a). During the first cycle, a certain area of H_{UPD} region is evident, while the CO oxidation peak is significantly suppressed, suggesting restricted contact between Pt and CO. In the second cycle of CV, the H_{UPD} region of E-Pt-CNT@SnO_2 remains almost the same as in the first cycle, with a minimal OH_{ad} region.

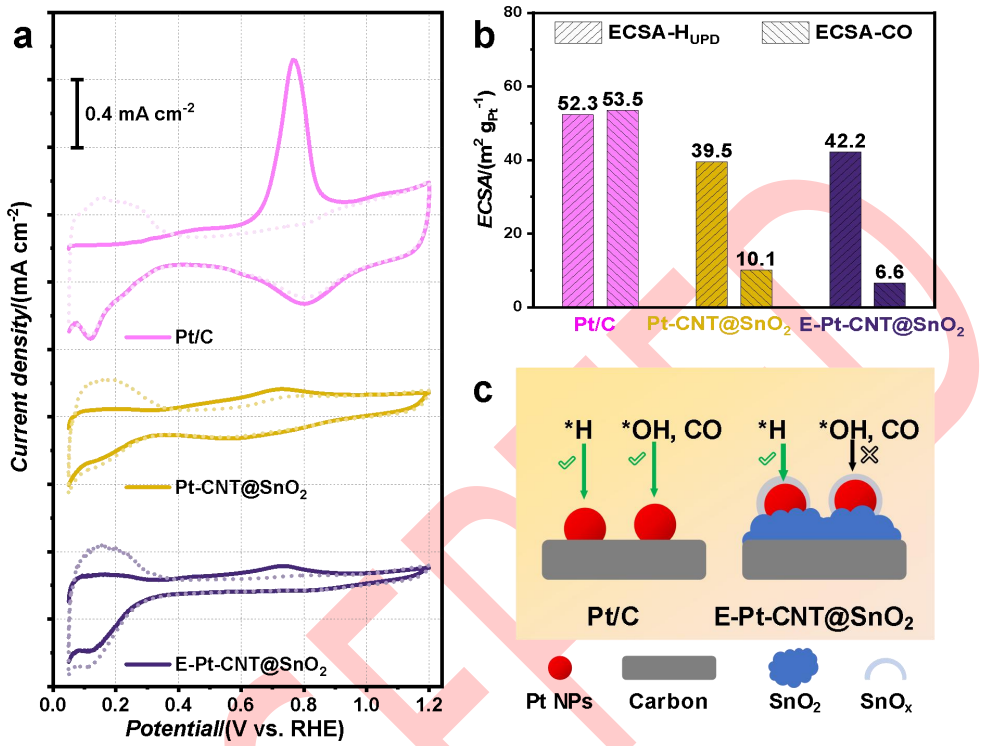

Figure 3. (a) CO-stripping curves of Pt/C, Pt-CNT@SnO_2 and E-Pt-CNT@SnO_2 in 0.1 M $HClO_4$ (scan rate: 20 mV·s^{-1}). The solid line represents the data from the first cycle, dotted line is the data of second cycle. (b) ECSA calculated from different method for Pt/C, Pt-CNT@SnO_2 and E-Pt-CNT@SnO_2. (c) Schematic illustration of the selective permeability of encapsulation layer due to the electrochemical-induced SMSI.

Furthermore, the Pt surface of Pt-CNT@SnO_2 should be exposed based on previous experimental results, but its electrochemical behavior is closer to that of E-Pt-CNT@SnO_2. This could be attributed to the low-potential treatment during the CO-stripping process, which might lead to a partial structural transformation towards E-Pt-CNT@SnO_2. The electrochemical surface areas (ECSA) of catalysts were calculated from the integrated areas of H_{UPD} region and CO oxidation peak (Figure 3b). It was observed that the ECSA-H_{UPD} and ECSA-CO_{ox} for Pt/C are very similar (52.3 vs. 53.5 $m^2 \cdot g_{Pt}^{-1}$). However, for E-Pt-CNT@SnO_2, there is a significant disparity in ECSA between these two methods (42.2 vs. 6.6 $m^2 \cdot g_{Pt}^{-1}$). This phenomenon further supports the validity of the hypothesis of electrochemically induced SMSI, which form the thin oxide encapsulation layer to prevent the CO adsorption on the surface of Pt NPs.

As depicted in schematic Figure 3c, due to the small size of protons and H_2 molecules, they can penetrate through the thin amorphous SnO_x layer. Consequently, E-Pt-CNT@SnO_2 exhibits a comparable ECSA-H_{UPD} to Pt/C. However, CO molecule is relatively larger than H_2 molecule and hard to penetrate the encapsulation layer,[33, 34] leading to a significantly smaller ECSA-CO_{ox} for E-Pt-CNT@SnO_2. Similarly, *OH molecule also struggles to permeate the oxide layer, which is the reason for the quite smaller OH_{ad} region area in the CV curve of E-Pt-CNT@SnO_2 than the H_{UPD} region. Furthermore, as O_2 molecules cannot effectively reach the Pt surface, E-Pt-CNT@SnO_2 exhibits a significantly inferior ORR activity to Pt-CNT@SnO_2 (Supporting Information Figure S5).

To further demonstrate the encapsulation of Pt NPs by SnO_x, E-Pt-CNT@SnO_2 was subject to the CV scanning in 0.1 M KOH to remove the SnO_x layer. After the alkaline treatment, the OH_{ad} region area of E-Pt-CNT@SnO_2 is observed (Supporting Information Figure S6), and the ORR activity is noticeably improved. This enhancement is attributed to the relatively poor alkaline resistance of SnO_x, and a portion of the amorphous SnO_x encapsulation layer on the surface of Pt is removed. In general, tradition thermal-induce SMSI is usually considered to be reversible on metal-oxides systems: supports could encapsulate the metal NPs under reducing conditions and the metal can be re-exposed under oxidizing conditions. Therefore, we attempted an electrochemical oxidation treatment on E-Pt-

CNT@SnO_2 through CV scanning between 1.0 to 1.6 V. However, the electrochemical oxidation process does not lead to a greater exposure of Pt surface in E-Pt-CNT@SnO_2 (Supporting Information Figure S7), and the reason needs further investigations.

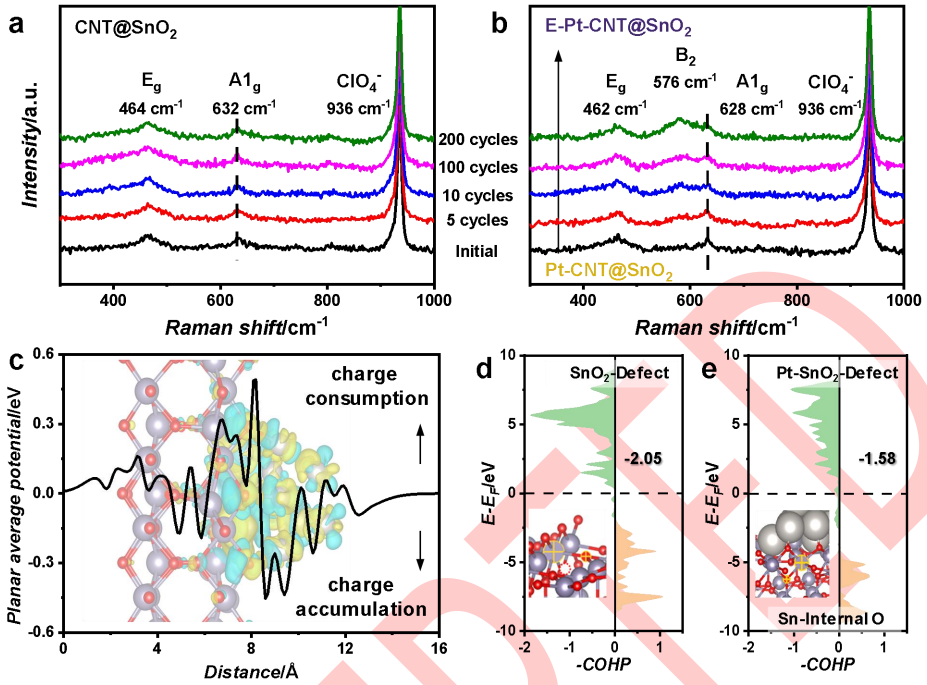

Figure 4. In-situ Raman spectra of (a) CNT@SnO_2 and (b)Pt-CNT@SnO_2. (c) Planar average charge density along the z-axis of Pt-SnO_2. Projected crystal orbital Hamilton population (pCOHP) for the Sn-O interaction in (d) defected SnO_2 and (e) Sn-Internal O in defected SnO_2 loaded with Pt.

Mechanism analysis of SMSI

Typically, inducing SMSI requires two essentials: one is the introduction of defects in the supports (such as H_2 treatment, UV radiation, shockwaves, or using chemical reducing agents) and another is promoting atomic migration through thermal energy or mechanical force. In the Pt-CNT@SnO_2 system, the electrochemical process can readily satisfy the first condition by inducing defects in the SnO_2 support. Considering the standard redox potentials of Sn (-0.138 V for Sn(0) → Sn(II) and 0.151 V for Sn(II) → Sn(IV)), the electrochemical treatment of Pt-CNT@SnO_2 is in a potential window of 0.05-1.2 V would lead to continuous redox of SnO_2. In-situ Raman spectra measurements (**Figure 4**a-b) suggest that the continuous redox process will not change the structure of CNT@SnO_2, especially the defect concentration in SnO_2. However, during the same process for Pt-CNT@SnO_2, the B_2 mode located around 576 cm^{-1} becomes more obvious, indicating the increment of defect concentration in SnO_2. The electron paramagnetic resonance (EPR) result is presented in Supporting Information Figure S8, indicating an increment of the concentration of oxygen vacancies within E-Pt-CNT@SnO_2. These results demonstrate the critical role of Pt in inducing defects in the SnO_2 support during the electrochemical treatment.

On the other hand, some studies suggest that the presence of noble metals could promote the migration of elements within the supports.[35, 36] As shown in Raman spectra, the location of A_{1g} mode in E-Pt-CNT@SnO_2 (628 cm^{-1}) exhibits a negative shift compared to that in CNT@SnO_2 (632 cm^{-1}). Since the A_{1g} and E_g modes of rutile SnO_2 reflect the Sn-O bond vibrations perpendicular to the z-axis, the negative shift of wavenumbers indicates the weakening of the Sn-O bond strength and that SnO_2 are more susceptible to defect formation in the presence of Pt. This makes electrochemically induced SMSI feasible at a room temperature.

Density functional theory (DFT) calculations are also employed to unveil interaction between Pt NPs and supports, including the electrons transfer and the bond strength. Given that Pt in E-Pt-CNT@SnO_2 only interfaces with SnO_2, the computational model has been simplified with the ignoring of CNTs. When Pt NPs are loaded onto SnO_2, electrons transfer from SnO_2 to Pt, leading to the formation of a charge consumption layer on SnO_2, as illustrated in Figure 4c. The number of bonding electrons between Sn and O should decrease, resulting in a significant decrease in the Sn-O bond energy around Pt NPs. To quantify the Sn-O bond strength, the integrating of the projected crystal orbital Hamilton population (IpCOHP) within the occupied states for the SnO_2 under different conditions were analyzed. The more positive the IpCOHP value indicates the weaker Sn-O bond strength. As shown in Figure 4d and Supporting Information Figure S9, the Sn-O bond strength is slightly reduced when the SnO_2 is defective. Moreover, when Pt is loaded on the defective SnO_2, the Sn-O bond strength is significantly reduced (Figure 4e and Supporting Information Figure S10). It is worth mentioning

that the bond strength between Sn atoms and the interior O atoms is weaker than that with surface O atoms. This facilitates the formation of small clusters of SnO_x around the Pt NPs. Subsequently, the small clusters migrate and realize the encapsulation of Pt NPs.

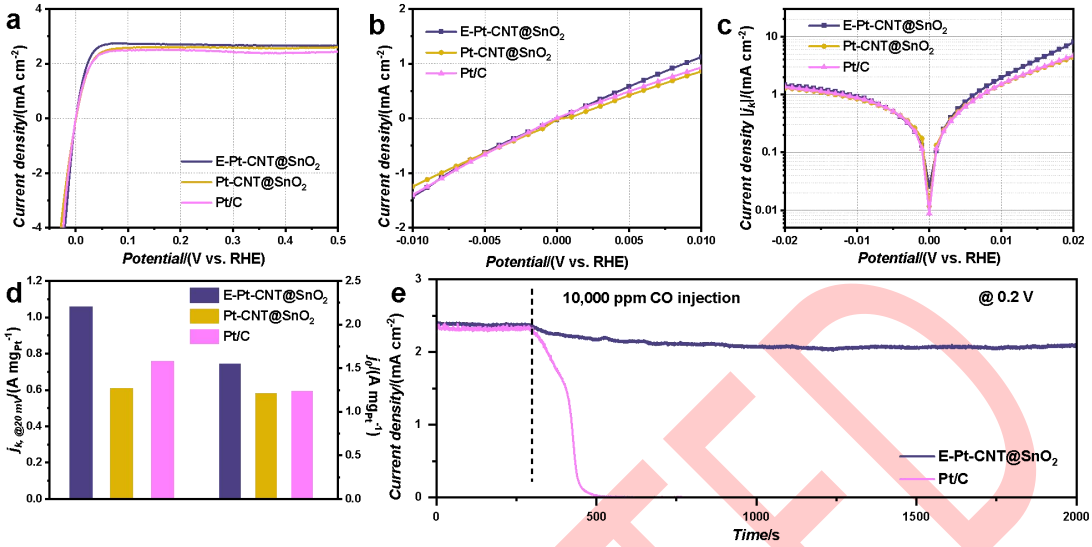

Figure 5. (a) HOR polarization curves of E-Pt-CNT@SnO_2, Pt-CNT@SnO_2 and commercial Pt/C in H_2-saturated 0.1 M $HClO_4$ (rotating speed, 1600 rpm; scan rate, 5 mV s^{-1}). (b) Micro region (-0.01 V - 0.01 V) of polarization curves. (c) Tafel plots of the kinetic current densities. (d) Comparison of mass and specific activities. (e) chronoamperometry curves with 10,000 ppm CO.

HOR performance

Since the obtained E-Pt-CNT@SnO_2 exhibits excellent resistance to CO but does not impact the penetration of H_2, its performance as a catalyst for HOR is evaluated. The HOR performance of E-Pt-CNT@SnO_2, Pt-CNT@SnO_2 and commercial Pt/C were investigated in H_2-saturated 0.1 M $HClO_4$ at a scan rate of 5 mV·s^{-1}. As shown in **Figure 5**a, the HOR polarization curve of E-Pt-CNT@SnO_2 exhibits the highest limit current density than that of Pt-CNT@SnO_2 and commercial Pt/C. The increased limiting current density of E-Pt-CNT@SnO_2 can be attributed to that the larger Pt-SnO_x interface and stronger interfacial hydrogen spillover from SnO_x to Pt surface. The micro region (-0.01-0.01 V) of polarization curves (Figure 5b) and the Tafel plots of kinetic current density (j_k) (Figure 5c) was plotted. The current density of E-Pt-CNT@SnO_2 increases faster with the potential, indicating the rapid reaction kinetics. The mass normalized j_k of E-Pt-CNT@SnO_2 at the overpotential of 20 mV is 1.06 A·mg_{Pt}^{-1}, which is higher than that of Pt-CNT@SnO_2 (0.61 A·mg_{Pt}^{-1}) and Pt/C (0.76 A·mg_{Pt}^{-1}). Moreover, the exchange current densities (j_0) based on the linear fitting of the polarization curves in the micro-polarized area by Butler-Volmer equation was calculated (Figure 5d and Supporting Information Figure S11). The j_0 of E-Pt-CNT@SnO_2 (1.55 A·mg_{Pt}^{-1}) is also higher than that of Pt-CNT@SnO_2 (1.22 A·mg_{Pt}^{-1}) and Pt/C (1.24 A·mg_{Pt}^{-1}), and it is the one of the best HOR catalyst in acidic media (Table S1). It has been studied that the electron transfer from SnO_x to Pt will downshift the *d*-band center of Pt and then weakens its adsorption energy with the H intermediate,[37, 38] which could account for the improved HOR activity of the catalyst.

Chronoamperometry tests were used to assess the tolerance of E-Pt-CNT@SnO_2 to CO (Figure 5e). Upon introducing 10,000 ppm of CO in H_2, the current density of Pt/C catalyst rapidly declined until complete deactivation within 300 s, as CO thoroughly poisoned the Pt sites. In contrast, E-Pt-CNT@SnO_2 exhibits a slower current density decay and maintains 85% of the current density preserved within 2000 seconds. This remarkable CO tolerance can be attributed to the effective protection of Pt sites from CO poisoning due to the electrochemical SMSI-induced SnO_x encapsulation layer.

Conclusion

In summary, we reported an electrochemical method to induce SMSI in Pt-CNT@SnO_2 system for CO-tolerant HOR. It was found that the CV scanning treatment can induce the dynamic structural evolution of catalyst, and HRTEM images proves that amorphous SnO_x layer covers Pt NPs. The E-Pt-CNT@SnO_2 encapsulated by amorphous SnO_x exhibits unique electrochemical properties with confined adsorption of CO but normal adsorption of H_2, which determine the excellent CO-tolerance of E-Pt-CNT@SnO_2 that can retain 85% current density for 2000 s under 10,000 ppm CO conditions. The electrons transfer from SnO_x to Pt NPs in E-Pt-CNT@SnO_2 improved the HOR activity, and the excellent exchange current density is 1.55 A·mg_{Pt}^{-1}. In addition, theoretical calculations and in situ Raman spectra reveal that the electrochemical redox operation and the charge transfer at a heterogeneous interface resulted in the weakening the Sn-O bond, which is the key of the occurrence of SMSI. This mild electrochemical-method provides

a new way for the design of supported catalysts, and also appeals attention to the evolution of structure during the electrochemical process of catalysts.

Supporting Information

The authors have cited additional references within the Supporting Information.[13, 39-45]

Acknowledgements

This research was financially supported by National Natural Science Foundation of China (22122202). The authors thank the Analytical and Testing Center of Huazhong University of Science and Technology (HUST) for carrying out the XPS, SEM, and TEM measurements.

References

[1] Van Deelen TW, Hernández Mejía C, de Jong KP. Control of metal-support interactions in heterogeneous catalysts to enhance activity and selectivity[J]. Nat. Catal., 2019, 2(11): 955-970.

[2] Li Y, Zhang Y, Qian K, Huang W. Metal-support interactions in metal/oxide catalysts and oxide-metal interactions in oxide/metal inverse catalysts[J]. ACS Catal., 2022, 12(2): 1268-1287.

[3] Tang H, Wei J, Liu F, Qiao B, Pan X, Li L, Liu J, Wang J, Zhang T. Strong metal-support interactions between gold nanoparticles and nonoxides[J]. J. Am. Chem. Soc., 2015, 138(1): 56-59.

[4] Luo Z, Zhao G, Pan H, Sun W. Strong metal-support interaction in heterogeneous catalysts[J]. Adv. Energy Mater., 2022, 12(37): 2201395.

[5] Tauster SJ, Fung SC, Garten RL. Strong metal-support interactions. Group 8 noble metals supported on TiO_2[J]. J. Am. Chem. Soc., 1978, 100(1): 170-175.

[6] Beck A, Huang X, Artiglia L, Zabilskiy M, Wang X, Rzepka P, Palagin D, Willinger MG, van Bokhoven JA. The dynamics of overlayer formation on catalyst nanoparticles and strong metal-support interaction[J]. Nat. Commun., 2020, 11(1): 3220.

[7] Zhang S, Plessow PN, Willis JJ, Dai S, Xu M, Graham GW, Cargnello M, Abild-Pedersen F, Pan X. Dynamical observation and detailed description of catalysts under strong metal-support interaction[J]. Nano Lett., 2016, 16(7): 4528-4534.

[8] Ro I, Resasco J, Christopher P. Approaches for understanding and controlling interfacial effects in oxide-supported metal catalysts[J]. ACS Catal., 2018, 8(8): 7368-7387.

[9] Zhang Y, Yan W, Qi H, Su X, Su Y, Liu X, Li L, Yang X, Huang Y, Zhang T. Strong metal-support interaction of ru on TiO_2 derived from the Co-reduction mechanism of $Ru_xTi_{1-x}O_2$ interphase[J]. ACS Catal., 2022, 12(3): 1697-1705.

[10] Wang L, Wang L, Meng X, Xiao FS. New strategies for the preparation of sinter-resistant metal-nanoparticle-based catalysts[J]. Adv. Mater., 2019, 31(50): 1901905.

[11] Pu T, Zhang W, Zhu M. Engineering heterogeneous catalysis with strong metal-support interactions: Characterization, theory and manipulation[J]. Angew. Chem. Int. Ed., 2022, 62(4): e202212278.

[12] Feng R, Li D, Yang H, Li C, Zhao Y, Waterhouse GIN, Shang L, Zhang T. Epitaxial ultrathin pt atomic layers on CrN nanoparticle catalysts[J]. Adv. Mater., 2023, 36(9): 2309251.

[13] Yang Z, Chen C, Zhao Y, Wang Q, Zhao J, Waterhouse GIN, Qin Y, Shang L, Zhang T. Pt single atoms on CrN nanoparticles deliver outstanding activity and CO tolerance in the hydrogen oxidation reaction[J]. Adv. Mater., 2023, 35(1): 2208799.

[14] Zhang Y, Liu JX, Qian K, Jia A, Li D, Shi L, Hu J, Zhu J, Huang W. Structure sensitivity of au-TiO_2 strong metal-support interactions[J]. Angew. Chem. Int. Ed., 2021, 60(21): 12074-12081.

[15] Tang HL, Su Y, Zhang BS, Lee AF, Isaacs MA, Wilson K, Li L, Ren YG, Huang JH, Haruta M, Qiao BT, Liu X, Jin CZ, Su DS, Wang JH, Zhang T. Classical strong metal-support interactions between gold nanoparticles and titanium dioxide[J]. Sci. Adv., 2017, 3(10): e1700231.

[16] Zhang X, Shi W, Li Y, Zhao W, Han S, Shen W. Pt_3Ti intermetallic alloy formed by strong metal-support interaction over Pt/TiO_2 for the selective hydrogenation of acetophenone[J]. ACS Catal., 2023, 13(7): 4030-4041.

[17] Wang X, Beck A, van Bokhoven JA, Palagin D. Thermodynamic insights into strong metal-support interaction of transition metal nanoparticles on titania: Simple descriptors for complex chemistry[J]. J. Mater. Chem. A, 2021, 9(7): 4044-4054.

[18] Liu S, Qi H, Zhou J, Xu W, Niu Y, Zhang B, Zhao Y, Liu W, Ao Z, Kuang Z, Li L, Wang M, Wang J. Encapsulation of platinum by titania under an oxidative atmosphere: Contrary to classical strong metal-support interactions[J]. ACS Catal., 2021: 6081-6090.

[19] Chen H, Yang Z, Wang X, Polo-Garzon F, Halstenberg PW, Wang T, Suo X, Yang SZ, Meyer HM, 3rd, Wu Z, Dai S. Photoinduced strong metal-support interaction for enhanced catalysis[J]. J. Am. Chem. Soc., 2021, 143(23): 8521-8526.

[20] Siniard KM, Li M, Yang SZ, Zhang J, Polo-Garzon F, Wu Z, Yang Z, Dai S. Ultrasonication-induced strong metal-support interaction construction in water towards enhanced catalysis[J]. Angew. Chem. Int. Ed., 2023, 135(20): e202214322.

[21] Hornberger E, Bergmann A, Schmies H, Kühl S, Wang G, Drnec J, Sandbeck DJS, Ramani V, Cherevko S, Mayrhofer KJJ, Strasser P. In situ stability studies of platinum nanoparticles supported on ruthenium-titanium mixed oxide (RTO) for fuel cell cathodes[J]. ACS Catal., 2018, 8(10): 9675-9683.

[22] Huang; R-Q, Liao; W-P, Yan; M-X, Liu; S, Li; Y-M, Kang; X-W. P-doped ru-pt alloy catalyst toward high performance alkaline hydrogen evolution reaction[J]. Journal of Electrochemistry, 2023, 29(5): 3.

[23] Chen; H-J, Tang; M-H, Chen S-L. Hydrophobicity optimization of cathode catalyst layer for proton exchange membrane fuel cell[J]. Journal of Electrochemistry, 2023, 29(9): 2.

[24] Liu X, Wang Y, Liang J, Li S, Zhang S, Su D, Cai Z, Huang Y, Elbaz L, Li Q. Introducing electron buffers into intermetallic pt alloys against surface polarization for high-performing fuel cells[J]. J. Am. Chem. Soc., 2024, 146(3): 2033-2042.

[25] Liu X, Zhao Z, Liang J, Li S, Lu G, Priest C, Wang T, Han J, Wu G, Wang X, Huang Y, Li Q. Inducing covalent atomic interaction in intermetallic pt alloy nanocatalysts for high-performance fuel cells[J]. Angew. Chem. Int. Ed., 2023, 62(23): e202302134.

[26] Kresse G, Furthmüller J. Efficient iterative schemes for ab initio total-energy calculations using a plane-wave basis set[J]. Phys Rev B, 1996, 54(16): 11169.

[27] Blöchl PE. Projector augmented-wave method[J]. Phys. Rev. B, 1994, 50(24): 17953.

[28] Perdew JP, Burke K, Ernzerhof M. Generalized gradient approximation made simple[J]. Phys Rev Lett, 1996, 77(18): 3865.

[29] Monkhorst HJ, Pack JD. Special points for brillouin-zone integrations[J]. Phys Rev B, 1976, 13(12): 5188-5192.

[30] Deringer VL, Tchougréeff AL, Dronskowski R. Crystal orbital hamilton population (cohp) analysis as projected from plane-wave basis sets[J]. The Journal of Physical Chemistry A, 2011, 115(21): 5461-5466.

[31] Patterson AL. The scherrer formula for x-ray particle size determination[J]. Physical Review, 1939, 56(10): 978-982.

[32] Geppert TN, Bosund M, Putkonen M, Stuhmeier BM, Pasanen AT, Heikkila P, Gasteiger HA, El-Sayed HA. HOR activity of Pt-TiO_{2-y} at unconventionally high potentials explained: The influence of SMSI on the electrochemical behavior of pt[J]. J. Electrochem. Soc., 2020, 167(8): 084517.

[33] Wang Y, Li Z, Zheng X, Wu R, Song J, Chen Y, Cao X, Wang Y, Nie Y. Renovating phase constitution and construction of pt nanocubes for electrocatalysis of methanol oxidation via a solvothermal-induced strong metal-support interaction[J]. Appl. Catal. B-Environ., 2023, 325: 122383.

[34] Jang J, Sharma M, Choi D, Kang YS, Kim Y, Min J, Sung H, Jung N, Yoo SJ. Boosting fuel cell durability under shut-down/start-up conditions using a hydrogen oxidation-selective metal–carbon hybrid core–shell catalyst[J]. ACS Appl. Mater. Interfaces, 2019, 11(31): 27735-27742.

[35] Fu Q, Colmenares Rausseo LC, Martinez U, Dahl PI, Garcia Lastra JM, Vullum PE, Svenum IH, Vegge T. Effect of sb segregation on conductance and catalytic activity at pt/sb-doped SnO_2 interface: A synergetic computational and experimental study[J]. ACS Appl. Mater. Interfaces, 2015, 7(50): 27782-27795.

[36] Wang Q, Gu Y, Zhu W, Han L, Pan F, Song C. Noble-metal-assisted fast interfacial oxygen migration with topotactic phase transition in perovskite oxides[J]. Adv. Funct. Mater., 2021, 31(40): 2106765.

[37] Li S, Liu J, Liang J, Lin Z, Liu X, Chen Y, Lu G, Wang C, Wei P, Han J, Huang Y, Wu G, Li Q. Tuning oxygen vacancy in SnO_2 inhibits pt migration and agglomeration towards high-performing fuel cells[J]. Appl. Catal. B-Environ., 2023, 320: 122017.

[38] Lin Z, Liu J, Li S, Liang J, Liu X, Xie L, Lu G, Han J, Huang Y, Li Q. Anti-corrosive SnS_2/SnO_2 heterostructured support for pt nanoparticles enables remarkable oxygen reduction catalysis via interfacial enhancement[J]. Adv. Funct. Mater., 2023, 33(11): 2211638.

[39] Samanta R, Mishra R, Barman S. Interface-engineered porous pt-PdO nanostructures for highly efficient hydrogen evolution and oxidation reactions in base and acid[J]. Acs Sustainable Chemistry & Engineering, 2022, 10(11): 3704-3715.

[40] Zhou Y, Yu F, Lang Z, Nie H, Wang Z, Shao M, Liu Y, Tan H, Li Y, Kang Z. Carbon dots/PtW_6O_{24} composite as efficient and stable electrocatalyst for hydrogen oxidation reaction in PEMFCs[J]. Chem. Eng. J., 2021, 426: 130709.

[41] Jin C, Wu F, Tang H, Pan H, Chen Z, Wang R, Meng Z, Li J, Tang H. Confined tuning of the charge distribution of pt electrocatalyst for reinforcing anti-poisoning ability: Toward efficient separation of hydrogen from gases containing ammonia[J]. Chem. Eng. J., 2023, 475: 146139.

[42] Chen G, Chen W, Lu R, Ma C, Zhang Z, Huang Z, Weng J, Wang Z, Han Y, Huang W. Near-atomic-scale superfine alloy clusters for ultrastable acidic hydrogen electrocatalysis[J]. J. Am. Chem. Soc., 2023, 145(40): 22069-22078.

[43] Li X, Han X, Yang Z, Wang S, Yang Y, Wang J, Chen J, Chen Z, Jin H. Lattice-distorted pt wrinkled nanoparticles for highly effective hydrogen electrocatalysis[J]. Nano Res., 2024: 1-8.

[44] Huang Z, Lu R, Zhang Y, Chen W, Chen G, Ma C, Wang Z, Han Y, Huang W. A highly efficient pH-universal HOR catalyst with engineered electronic structures of single pt sites by isolated Co atoms[J]. Adv. Funct. Mater., 2023, 33(47): 230633.

[45] Zhou YY, Xie ZY, Jiang JX, Wang J, Song XY, He Q, Ding W, Wei ZD. Lattice-confined ru clusters with high CO tolerance and activity for the hydrogen oxidation reaction[J]. Nat. Catal., 2021, 4(4): 341-341.

Entry for the Table of Contents

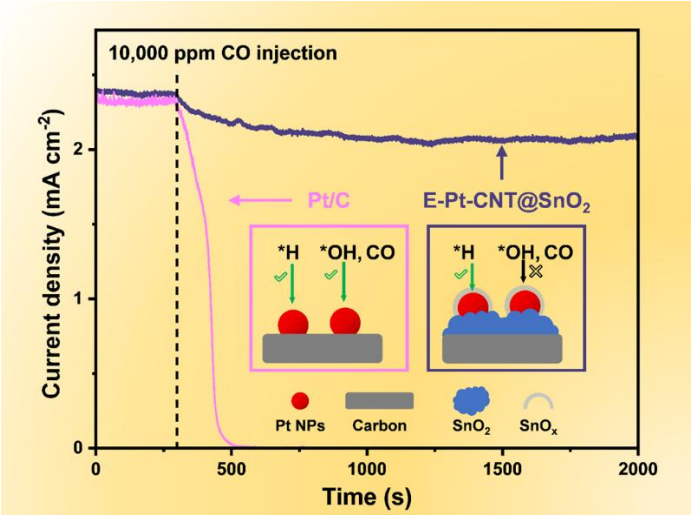

电化学方法诱导强金属-载体相互作用提高氢氧化反应催化剂的 CO 耐受性

李申宙[a,+]，林子杰[a,+]，陈麒安[a,+]，蔡钊[b]，李 箐[a,*]

[a]材料成形与模具技术国家重点实验室，材料科学与工程学院，华中科技大学，湖北 武汉 430074

[b]材料科学与化学学院，中国地质大学（武汉），湖北 武汉 430074

摘要：诱导经典强金属-载体相互作用（SMSI）是一种提高负载型金属催化剂性能的有效途径，这指的是载体包覆金属纳米颗粒的结构重构效应。传统的 SMSI 诱导方式是热还原方法，但这过程中往往伴随着会损害催化活性的金属纳米颗粒的长大过程。为了解决这一问题，本研究开发了一种温和的电化学方法来诱导 SMSI，并在核壳结构 CNT@SnO_2 载体上负载的 Pt 纳米颗粒催化剂中进行了验证。高分辨透射电镜（HRTEM）和电化学测试结果证实了电化学诱导方法成功在 Pt 纳米颗粒表面构建了 SnO_x 包覆层。这种 SnO_x 包覆层可以保护 Pt 纳米颗粒在氢氧化反应（HOR）中不受 CO 杂质的毒害。实验显示，当 H_2 中混入 10000 ppm 浓度的 CO 时，E-Pt-CNT@SnO_2 的 HOR 电流密度经过 2000 s 后仍能保持 85%，而商用 Pt/C 在相同条件条件下工作 300 s 则完全失活。此外，SnO_x 包覆层与 Pt 纳米颗粒之间存在电子相互作用，这导致电荷从载体迁移到 Pt 纳米颗粒上，并在远离界面处聚集。这种电荷转移降低了 Pt 对 H 中间体的吸附能，提高了 E-Pt-CNT@SnO_2 的 HOR 活性，催化剂的交换电流密度为 1.55 $A \cdot mg_{Pt}^{-1}$，是商业 Pt/C 的 1.3 倍。原位拉曼光谱和理论计算结果表明，电化学诱导 SMSI 的关键因素是 Pt 纳米颗粒对 Sn-O 键强度的减弱。此外，Pt 纳米颗粒对载体不同区域的 Sn-O 键强度的弱化存在差异，其中表面 Sn 原子与内部 O 原子之间的键强度弱于 Sn 原子与表面 O 原子之间的键强度，这促进了 SnO_x 团簇的形成和迁移。

关键词：强金属-载体相互作用；铂纳米颗粒；氢氧化反应；负载型催化剂；CO 耐受性